



Supplementary Materials for

The stress-sensing domain of activated IRE1 α forms helical filaments in narrow ER membrane tubes

Ngoc-Han Tran *et al.*

Corresponding authors: Peter Walter, peter@walterlab.ucsf.edu; Grant J. Jensen, grant_jensen@byu.edu

Science **374**, 52 (2021)
DOI: 10.1126/science.abh2474

The PDF file includes:

Materials and Methods
Figs. S1 to S14
References

Other Supplementary Material for this manuscript includes the following:

MDAR Reproducibility Checklist
Movies S1 to S3

Materials and Methods

Cell culture and grid preparation

Previously described MEFs-IRE1 α -mNG and U2OS-IRE1 α -mNG cell lines (14, 24) were cultured in high glucose DMEM media supplemented with 10% tetracycline-free fetal bovine serum (FBS; Takara Bio), 6 mM L-glutamine, and 100 U/ml penicillin/streptomycin. All cell lines used in the study tested negative for mycoplasma contamination when assayed with the Universal Mycoplasma Detection Kit (ATCC 30-1012K). To minimize autofluorescence, the same culture media without phenol red was used to grow cells for grid preparation (27). Prior to cell plating, gold Quantifoil London finder grids (EMS R2/2 LF-Au-NH2) were UV treated to sterilize and coated with cell adhesion matrix. For MEFs- IRE1 α -mNG cell line, grids were coated in droplets of 500 μ g/mL Fibronectins (Sigma-Aldrich S5171-.5MG) for 5 minutes on each side, washed in PBS, blotted and air-dried. For U2OS- IRE1 α -mNG cell line, grids were coated with \sim 4 mg/mL undiluted Collagen type I (Corning 354236) droplets for 20 minutes, washed in PBS, blotted and air-dried. Cells were seeded at 15% confluence and allowed to adhere for 8 hours and induced with Doxycycline (500 nM) for 6 or 18 hours for MEFs and U-2 OS cell lines, respectively. At this induction level, IRE1 α -mNG is overexpressed \sim 10-fold over endogenous IRE1 α expression in these cells at an estimate of \sim 100 000 molecules per cell (24). ER stress was then induced by treatment with 1.5 μ g/mL of tunicamycin for 2 hours, which effectively recapitulated IRE1 α induction (24). For technical reasons, tunicamycin was used in all the CLEM/ET experiments. The morphology and dynamics of IRE1 α clusters induced by other ER stressors such as thapsigargin were indistinguishable from those formed with tunicamycin treatment (24).

Immediately prior to being plunge frozen, 3 μ l of a beads suspension was added to the grids. The bead suspension was made by a 1:1 dilution of 500 nm blue (345/435 nm) polystyrene fluorospheres (Phosphorex) with a 3:1 concentrated solution of 20 nm:5 nm colloidal gold (Sigma Aldrich) blocked with 5% bovine serum albumin. The gold beads served as fiducial markers for cryo-tomogram reconstruction while the blue fluorospheres served as landmarks for registering cryogenic fluorescence microscopy images collected from different channels as well as with cryo-EM projection images for cryo-CLEM (27). Residual media and bead suspension were blotted manually from the back side with Whatmann paper #40 in 90% humidity. Grids are plunge-frozen in liquid ethane/propane mixture using a Vitrobot Mark IV (FEI, Hillsboro, OR). This vitrification method results in good preservation of cellular structures in most of the cytoplasm. Thicker regions such as nuclei, not examined here, show less complete vitrification. Plunge-frozen grids were subsequently loaded into Polara EM cartridges (FEI) (26). Cryo-EM cartridges containing frozen grids were stored in liquid nitrogen and maintained at ≤ -150 $^{\circ}$ C throughout the experiment including cryogenic fluorescence microscopy imaging, cryo-EM imaging, storage and transfer.

Fluorescence imaging and image processing

The EM cartridges were transferred into a cryo-FLM stage (FEI Cryostage), modified to hold Polara EM cartridges (26), and mounted on a Nikon Ti inverted microscope. The grids were imaged using a 60X extra-long-working-distance air-objective (Nikon CFI S Plan Fluor ELWD 60X NA 0.7 WD 2.62–1.8 mm). Images were recorded using a Neo 5.5 sCMOS camera (Andor Technology, South Windsor, CT) using a 2D real-time deblur deconvolution module in the NIS Elements software from AutoQuant (Nikon Instruments Inc., Melville, NY). The 2D real-time

deconvolution algorithm estimates a PSF using several factors such as sample thickness, noise levels in the image, background subtraction and contrast enhancement. All fluorescence images (individual channels) were saved in 16-bit grayscale format. IRE1 α -mNG was visualized with a GFPHQ filter set (Semrock; Ex455-485, DM 495, Em 500-545nm). Blue fluorospheres were visualized with a DAPI filter set (Semrock; Ex340-380, DM 400, Em 435-485nm). Red autofluorescence was imaged using a TxRed filter set (Semrock; Ex540-580, DM 595, Em 600-660nm).

EM imaging

Cryo-EM grids previously imaged by cryo-LM were subsequently imaged by electron cryotomography using a FEI G2 Polara 300 kV FEG TEM (FEI) equipped with an energy filter (slit width 20 eV for higher magnifications; Gatan, Inc.), and a 4 k \times 4 k K2 Summit direct detector (Gatan, Inc.) in counting mode.

IRE1 α -mNG foci targets were defined as spots with at least 25-fold higher fluorescence in green channel than both red and blue fluorescence. Spots meeting these criteria are absent in control samples. First, cellular areas containing the fluorescent bodies of interest in suitably-thin areas that were typically 200-500 nm thick were located in the TEM using methods described previously. Tilt series were then recorded of these areas using UCSF Tomography (39) or SerialEM (40) software at a magnification of 27,500X for MEFs-IRE1 α -mNG (Polara) and 34,000X for U2OS-IRE1 α -mNG (Polara). This corresponds to a pixel size of 3.712 Å (MEFs-IRE1 α -mNG) or 3.260 Å (U2OS-IRE1 α -mNG), respectively, at the specimen level and was found to be sufficient for this study. Each tilt series was collected from -60° to $+60^\circ$ with an increment of 1° in an automated fashion at 4–10 μ m underfocus. The cumulative dose of one tilt-series was between 80 and 150 e $^-$ /Å 2 . The tilt series was aligned and binned by 4 into 1k x 1k using the IMOD software package (41), and 3D reconstructions were calculated using the simultaneous reconstruction technique (SIRT) implemented in the TOMO3D software package (42), or weighted back projection using IMOD. Noise reduction was performed using the non-linear anisotropic diffusion (NAD) method in IMOD (41), typically using a K value of 0.03–0.04 with 10 iterations.

Segmentation and isosurface generation

Segmentation and isosurface rendering were performed in Amira (Thermo Scientific). For lower resolution tomograms from MEFs cells, the segmentation was done all manually using the brush, lasso, and thresholding tools combined with interpolation and surface smoothing. For higher resolution tomograms from U2-OS cells, the ER, IRE1 α subdomains and vesicles were segmented manually. Cytoskeletal components and ribosomes were segmented using the TomoSeg CNN module in EMAN2 (43). For U2-OS tomograms, the TomoSeg CNN module was also trained to segment parallel membrane densities characteristic of narrow IRE1 α subdomain tubes to verify the general features of manual segmentation. Although both segmentation methods can be impacted by subjective bias, the manual segmentation and TomoSeg training were performed by different people and done independently.

Conventional electron microscopy

HEK293 stable cells expressing IRE1 α -GFP, unstressed or treated with tunicamycin, were fixed with 2.5 % glutaraldehyde, 2% paraformaldehyde in 0.1 M Sorenson's phosphate buffer (PB), pH 7.4, for 2 h at room temperature. After storage in 1% PFA, 0.1 M PB at 4 °C for about 1

week and rinsing in 0.1 M PB, the cells were postfixed with 1 % OsO₄ and 1.5 % K₃Fe(CN)₆ in 0.07 M PB, stained *en bloc* in aqueous 0.5 % uranyl acetate, dehydrated in acetone and embedded in Epon. Ultrathin plastic sections were stained with uranyl acetate and lead citrate and examined in a JEOL JEM-1010 electron microscopy. An estimated of 100 cells were screened per condition, and each micrograph analyzed was derived from a unique cell.

Immuno-electron microscopy

HEK293 cells stably expressing IRE1 α -GFP, untreated or treated with tunicamycin, were fixed using 4 % PFA in 0.1 M PB for 2 h at room temperature, then overnight at 4 °C. Subsequently, the fixation was continued by replacing the initial fixative with 1 % PFA in 0.1 M PB for several days. The samples were then rinsed in PBS, blocked with 0.15 % glycine in PBS, scraped in 1% gelatin in PBS, pelleted, and embedded in 12 % gelatin. Small blocks of pellet were cryoprotected with 2.3 M sucrose, mounted on aluminum pins and frozen in liquid nitrogen. Ultrathin cryosections were cut at -120 °C, placed on copper carrier grids, thawed and immunolabeled as previously described (44). In brief, the sections were incubated with blocking buffer containing fish skin gelatin (Sigma-Aldrich, G7765) and acetylated BSA (Aurion, 900.022) and immunolabeled with biotinylated goat anti-GFP antibody (Rockland, 600-106-215) at 1:300, followed by rabbit anti-biotin antibody (Rockland, 100-4198) at 1:10000. Subsequently, the sections were incubated with Protein A-conjugated 10 nm gold particles (Cell Microscopy Core, University Medical Center Utrecht, the Netherlands), stained with uranyl acetate followed by a methylcellulose-uranyl acetate mixture, and examined in a JEOL JEM-1010 electron microscope. An estimated of 100 cells were screened per condition, and each micrograph analyzed was derived from a unique cell.

This labeling method is relatively bulky (45) and could result in immunogold particles that are estimated to be up to 25 nm away from the GFP epitope fused to IRE1 α 's cytosolic linker. In addition, only thin 2-D sections are visualized and labelled, which could result in immunogold particles labeling without visible membranes nearby. In combination with the expected sparse labeling of immunogold particles, the interpretation of this method is limited to the labeling of regions enriched in narrow tubes rather than labeling individual IRE1 α -GFP molecules.

Subtomogram averaging

In U2OS cells each tilt series was collected from -60° to +60° with an increment of 1° in an automated fashion using SerialEM at 4–6 μ m underfocus. The image pixel size used for subtomogram averaging was 6.52 Å (binned by 2). Subsequent subtomogram averaging was performed by the EMAN2 tomography pipeline (46). Initially unbinned tilt-series were automatically aligned and reconstructed using EMAN2. In total, 3 cryo-tomograms were generated to provide a sufficient number of particles for further processing. Particles were picked using EMAN2 particle picking software using a box size of 56x56x56 pixels. Briefly model points were placed every 10 nm along the length (approximately one helical turn), of the oligomer present inside the membrane tube. Particles of various orientations were picked, including top-views and side-views. In total 653 model points were picked. CTF estimation and correction was performed by EMAN2. An initial model was then generated in C1 with all 653 particles in 5 iterations. The iteration 5 map was aligned to the symmetry axis and was used as an initial model for subtomogram refinement using C2 and D2 symmetry. The first iteration D2 map generated in subtomogram refinement was used as a reference for a sub-tilt refinement step using helical symmetry in 5 iterations. The helical symmetry parameters were as follows; C

symmetry = 2, rotation about the Z axis = 45°, nsym = 2.5, and tz = 5. The map produced by iteration 5 includes 80% of the best aligned particles and is shown in figure S10. To focus on one strand of the helix, an automatic mask was generated to improve alignment in 5 iterations. The one-stranded map produced by iteration 5 includes 80% of the best aligned particle and is shown in figure 4. The particles were split into two subsets and resolution is measured by the Fourier shell correlation of these two density maps. The correct hand of the final map was determined by EMAN2 and confirmed by subtomogram averaging of ribosomes in the same tomograms. The particles were mapped back into the cryo-tomogram by EMAN2 using a pKeep of 0.6.

Model prediction and oligomer generation

Two independent methods were used to build a human IRE1 α -LD oligomer: (Method 1) based on protein threading of the human IRE1 α -LD sequence into the yeast IRE1 2BE1 crystal structure or (Method 2) by generating an active human IRE1 α -LD model by SWISS-MODEL homology modeling (47). Both resulting models accounts well for the averaged map of the luminal density. The threaded model is shown in all main and supplementary figures, while the SWISS-Model is shown in the supplementary movies.

For Method 1 (Fig S11), we used the previously-published model of a human IRE1 α -LD monomer (14), which was produced by threading the human IRE1 α sequence (residues 24-366; Uniprot entry O75460) into the *S. cerevisiae* luminal domain crystal structure (PDB:2BE1) with the I-TASSER server (28). Using the I-TASSER server “Option 1,” the 2BE1 crystal structure was assigned as the template to guide the modelling. A tetramer was then built by superimposing four modeled monomers onto the *S. cerevisiae* tetramer where the dimer:dimer interface is observed in the extended crystal contact. The modeled human tetramer was then fitted into the sub-tomogram average cryo-EM density map using the “fit in map” function of Chimera, optimizing the fit for one dimer. Keeping the dimer interface constant, the interface between adjacent dimers was adjusted to optimize the fit of the second dimer (Fig S11H). A higher order oligomer was built by duplicating the new tetramer and using the “match” function in Chimera to propagate the helical oligomer. Nine monomers of the resulting helix completed one turn, and the fit values reported reflect the output of the “fit in map” function applied to all 9 monomers. Minor sidechain clashes at the dimer:dimer interface exist and are resolvable by side chain bond rotations, but lacking the resolution in the cryo-EM map to resolve such details or even the secondary structures at the interface, we chose not to resolve them.

For Method 2, SWISS-MODEL was used to predict the human active dimer of IRE1 α , also based on the human sequence and the *S. cerevisiae* IRE1-LD crystal structure (PDB:2BE1) as a template. To prepare the template for SWISS-MODEL, the missing loops in the crystal structure were built using Modeller in Chimera (48). Two predicted model IRE1 α dimers were superimposed onto the *S. cerevisiae* IRE1-LD crystal structure dimer-dimer in Chimera. The *S. cerevisiae* IRE1-LD crystal structure dimer-dimer was then omitted, leaving a gap between the two predicted human IRE1 α dimers. A new interface was modelled in Chimera by translating one dimer along one axis until the gap was filled. To accommodate the new dimer-dimer interface in the double-helical map, the angle between the two dimers was made more acute to approximately 45° (the rise of the helix). The resulting dimer was then placed into the map using the fit-to-map function in Chimera. The remainder of the helix was then built while maintaining the same dimer-dimer interface throughout the helix.

Quantifications

IRE1 α subdomain tube diameters from cryo-CLEM-ET experiments were measured by drawing lines between the center of each membrane density perpendicular to tube membranes in IMOD (41). Regions less than 30 nm away from a junction are excluded. Tube diameters for 12 representative tomograms from 7 cells in 4 biological replicates were quantified as 409 measurements. The distance outputs from IMOD have at least 4 significant figures, but only two significant figures are reported for the average diameter to reflect the degree of variation (\pm 3.056 nm; standard deviation).

Quantification of ribosome distances in Fig. S4 was performed by stepping along visible membranes in XY plane and manually measuring the distance between the membrane cytosolic edge to the outer edge of the nearest clearly visible ribosome. Ribosomes whose membrane tangent lines intercept other ribosomes are excluded as belonging to an outer layer. Each distance measurement was binned as either “IRE1 α subdomain” or “ER membrane” based on the membrane assignment from manual segmentation. The reported measurement numbers (N = 218, 180, 215, 519) are for unique ribosomes visible across multiple Z planes per bin per tomogram.

Quantifications of the diameters of IRE1 α subdomain tubes and ER cisternae for conventional and immuno-electron microscopy were performed using Fiji software (49). Diameters of IRE1 α subdomain tubes were measured as both longitudinal and end-on cross sections. In each micrograph, measurements were obtained perpendicular to the membranes from the cytosolic edges of each membrane density every 30-50 nm as long as both membranes were clearly visible. Measurement outputs have at least three significant figures, but only two are reported for averaged IRE1 α subdomain tubes diameters to reflect the standard deviations.

Distributions of immunogold particles shown in Fig. 2 were generated by manually extracting the X-Y coordinates of each gold particle and using a python script to measure all pairwise distances and plotting the distance distribution. 8 and 14 micrographs were used for non-stressed and stressed samples, respectively. In total, 238 inter-particle distances were extracted from non-stressed micrographs and 1553 distances from stressed micrographs.

Intensity line plots shown in Fig. 3 were generated by averaging and aligning multiple line plots across each subdomain cross section. Nine cross sections from 4 tomograms obtained in 2 biological replicates in MEF-mNG cells were used. The resulting averaged plots were subsequently aligned and averaged as shown in Fig. 3C. Line plots from each cross section were aligned either at the center trough in density or by finding peaks of membrane densities to center the alignment. Both methods were tested, and the alignment method generating the smaller error of the means were chosen. The exact alignment parameters can be found in the deposited analysis code (38).

Quantification of radii of curvature was performed in Fiji (49) by dividing IRE1 α subdomain tubes clearly visible in XY planes into tiling 25 nm segments, excluding junctions. Circles with diameters in increments of 50 nm were then manually fitted to each segment to yield estimates of the radius of curvature. 274 radii of curvature were extracted and plotted in the histogram.

Calculations

Calculations of IRE1 α domain concentration assumes IRE1 α subdomain tubes to be perfect cylinders of 28.3 nm diameter measured from membrane centers with a membrane thickness of 37.5 Å (50). The threaded and SWISS-homology oligomeric model show 9 and 12 monomers per turn per strand, respectively. All calculations use both values as lower and upper bounds,

resulting in each 100 nm filament within 100 nm membrane cylinder contains 104-139 IRE1 α -LD monomers, approximated from a pitch of 173 Å with 18 or 24 monomers per turn. Either a range or an averaged approximation are reported in the main text.

The volume occupied by IRE1 α -LD is calculated by using a glycosylated MW of 49196 g/mol and a density of 1.35 g/mL (51), yielding a volume of 6.292×10^3 or 8.41×10^3 nm³ occupied by 104 or 139 IRE1 α -LD monomers and 4.09×10^4 or 3.87×10^4 nm³ void volume, respectively. In this void volume, a single substrate molecule has a concentration of 41-43 μ M. IRE1 α density fold change upon stress is approximated from 104 or 139 monomer per 0.008890 μ M² and contrasting to earlier calculations (24), yielding 11700 to 15600 molecules per μ M².

Because the presence of long and predicted unstructured linkers on the luminal and cytosolic side (52 and 105 amino acid, respectively) provides sufficient translational and rotational freedom, we also estimate the effective 3D concentrations. IRE1 α -LD concentration is extracted from the molarity of 104 or 139 units as 1.73×10^{-22} or 2.31×10^{-22} mole / 4.7144×10^{-20} L, yielding concentrations of 3700 and 4900 μ M, respectively. IRE1 α cytosolic domain concentrations of 170-220 μ M are estimated from the approximate volume experienced by this domain (1.05×10^6 nm³ which assumes the domain extends 44 nm from the membrane due to a stretched cytosolic linker + KR domain height from crystal structures). Estimation of molecular weight cut-off for accessibility of other molecules in IRE1 α subdomain tubes assumes the largest diameter of accessible space is 6 nm, which is the distance between the membrane luminal boundary and the outer boundary of IRE1 α luminal filament. For a perfectly spherical protein with a radius of 3 nm and a density of 1.35 g/mL, its molecular weight can have an upper bound of ~90 kDa.

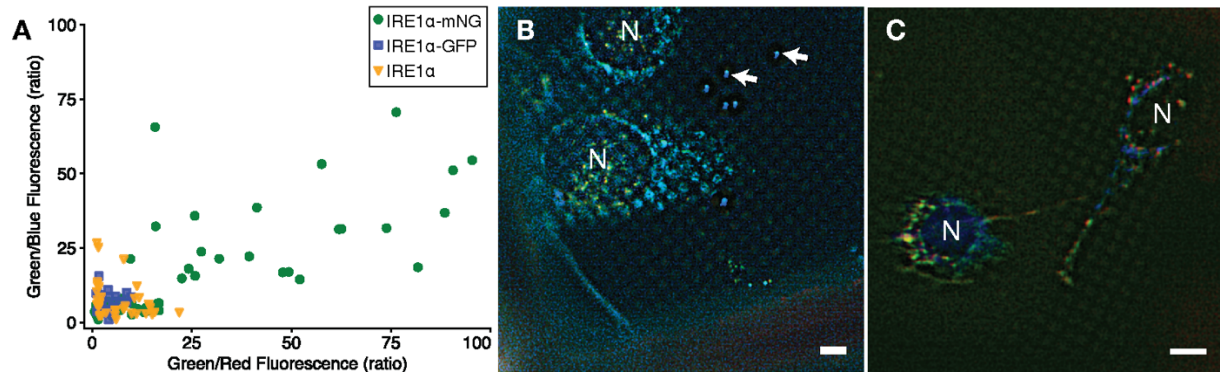


Fig. S1.

Fluorescent profile across cell lines expressing different IRE1 α constructs. (A) Scatter plot of fluorescent profiles for bright spots observed at liquid nitrogen temperature for stressed cells expressing IRE1 α -mNG, IRE1 α -GFP or WT IRE1 α . The ratios of Green/Red and Green/Blue fluorescence intensity taken at the same exposures across channels are used to identify specific IRE1 α signal. IRE1 α -mNG foci targets were defined as spots with at least 25-fold higher fluorescence in green channel than both red and blue fluorescence. Spots meeting these criteria are absent in control samples. Representative cryo-fluorescent light microscope images of stressed MEFs-IRE1 α -GFP (B) and MEFs-IRE1 α (C; lacking fluorescent protein) cells grown directly on coated Quantifoil grids imaged at 1 second exposure in BFP, GFP and mCherry channels. Cells were treated with Tm for 2 hours prior to cryo-preservation and imaged in liquid nitrogen. Nuclei are indicated with "N." White arrows: 500 nm fluorescent nanosphere. Scale bars are 6 μ m.

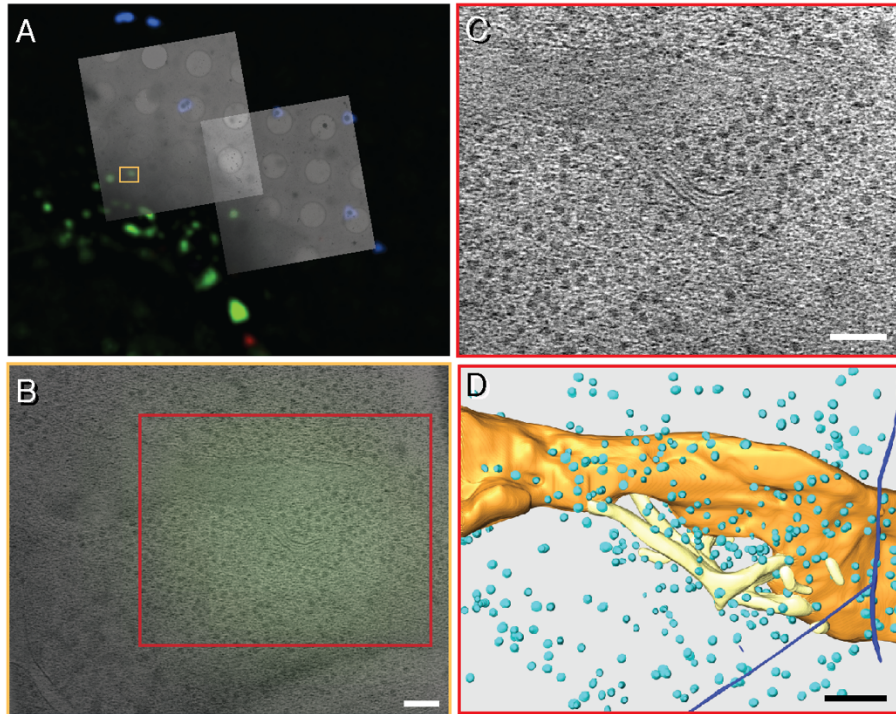


Fig. S2.

Target identification by correlation and tomographic reconstruction in intact MEFs cells expressing IRE1 α -mNG. (A) Overlay of multi-channel cryo-LM images with low magnification (3000X) cryo electron micrographs of regions containing IRE1 α -mNG foci formed after 2 hours ER stress induction. Blue fluorescent spheres visible by both light and electron microscopy were used to align the images in X and Y directions prior to targeting cell regions for high magnification tilt series. (B) Correlation of reconstructed tomogram with fluorescent signal reveals sub-regions with IRE1 α foci in an additional example from the same cell depicted in Fig. 1B-F. (C) A z slice showing thin membrane tubes within regions colocalizing with IRE1 α -mNG signal. (D) manual 3D segmentation for tomogram in C. Orange: normal ER membrane. Yellow: thin ER membranes at IRE1 α -mNG regions. Teal: ribosomes. Blue: cytoskeletal elements. Scale bars: 100 nm.

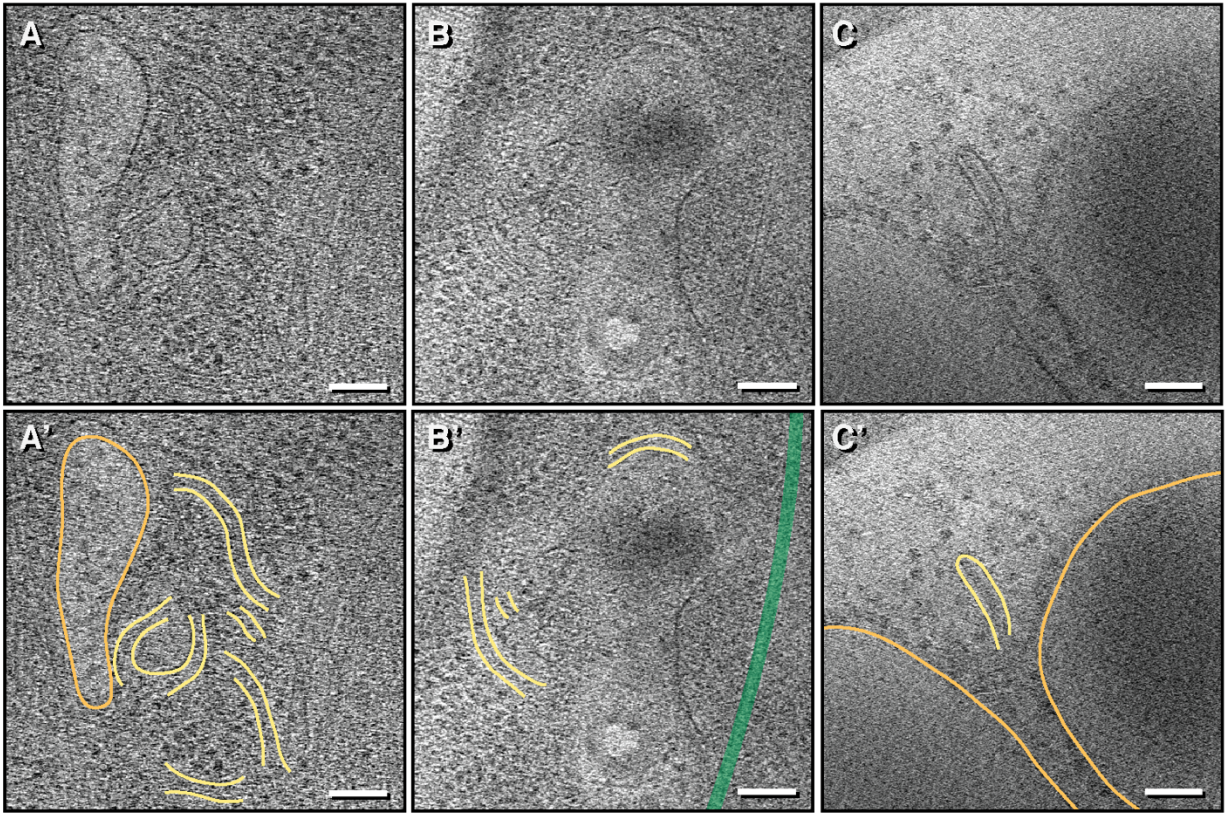


Fig. S3.

Additional example of IRE1 α -mNG fluorescence correlated to narrow membrane tubes in stressed MEFs-IRE1 α -mNG cells. (A-C) Representative z slice of corresponding sub-regions correlated with IRE1 α -mNG signal in 3 different examples obtained in stressed cells expressing IRE1 α -mNG. Scale bar = 100 nm. (A'-C') Segmentation of membranes and structures observed in tomograms where yellow = thin ER tubes of IRE1 α subdomains, orange = membrane of ER sheet/tubules, and green = cytoskeletal components.

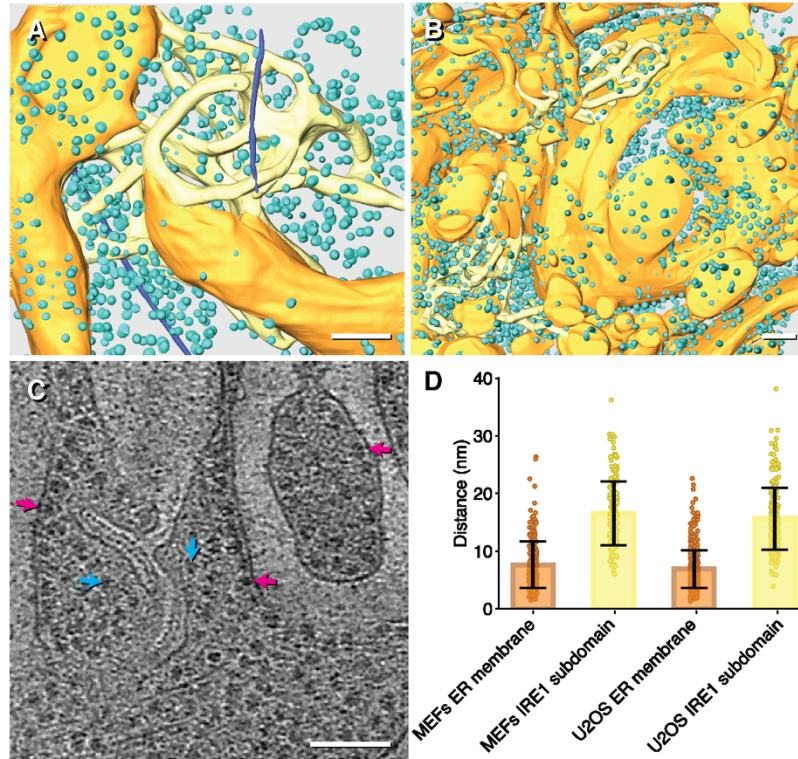


Fig. S4.

IRE1 α subdomain tubes are devoid of bound ribosomes. (A) Segmentation of MEFs tomogram corresponding to Fig. 1D but showing ribosomes and cytoskeletal segmentation. Scale bar = 100 nm (B) Segmentation of U2OS tomogram with larger cell region corresponding to Fig 1F with ribosomes and cytoskeletal components shown. Scale bar = 100 nm. (C) An example z slice of IRE1 α subdomain tube and adjacent ER sheet/tubules. Cyan arrows point to ribosomes near IRE1 α subdomains; Magenta arrows indicate ribosomes bound to ER membranes. Scale bar = 100 nm. (D) Plot of distance between ribosomes and membranes comparing ER sheet/tubules membranes and IRE1 α subdomain membranes for tomograms in A and B. Distances were measured by stepping along visible membranes in XY plane and manually measuring the distance between the membrane cytosolic edge to the outer edge of the nearest clearly visible ribosome. Error bar is standard deviation. n = 218, 180, 215, 519 measurements.

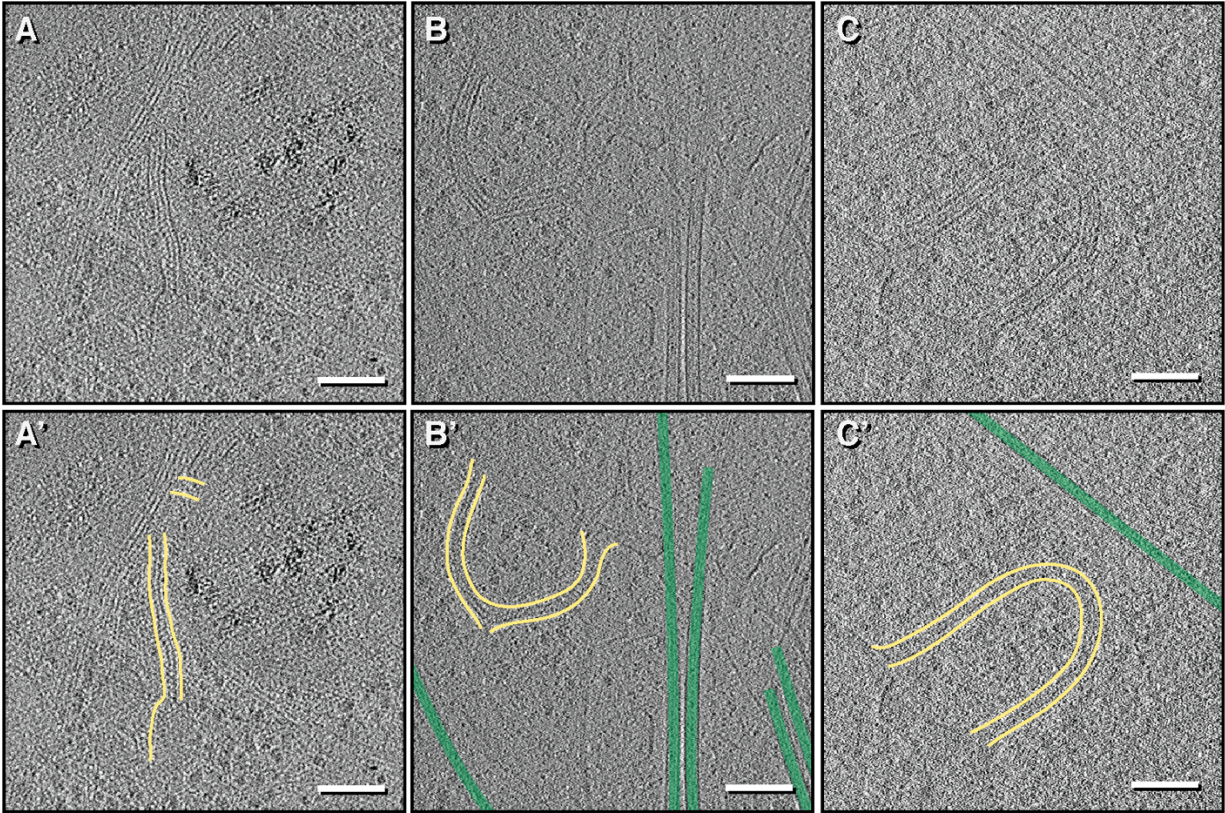


Fig. S5.

Additional example of IRE1 α fluorescence correlated to narrow membrane tubes in stressed U2OS cells expressing fluorescently tagged IRE1 α . (A-B) Representative z slice from two additional examples obtained in stressed U2OS-IRE1 α -mNG cells expressing fluorescently tagged IRE1 α . (C) representative Z slice from an example obtained from U2OS-IRE1 α -mRuby cell line where IRE1 α is tagged at same location with an mRuby3 red fluorescent protein instead of mNG. Observation of narrow membrane tubes with specific red fluorescence using mRuby3 supports that bright fluorescent foci are indeed IRE1 α foci rather than autofluorescent signal. (A'-C') Segmentation of membranes and structures observed in tomograms where yellow = thin ER tubes of IRE1 α subdomains and green = microtubules. Scale bar = 100 nm.

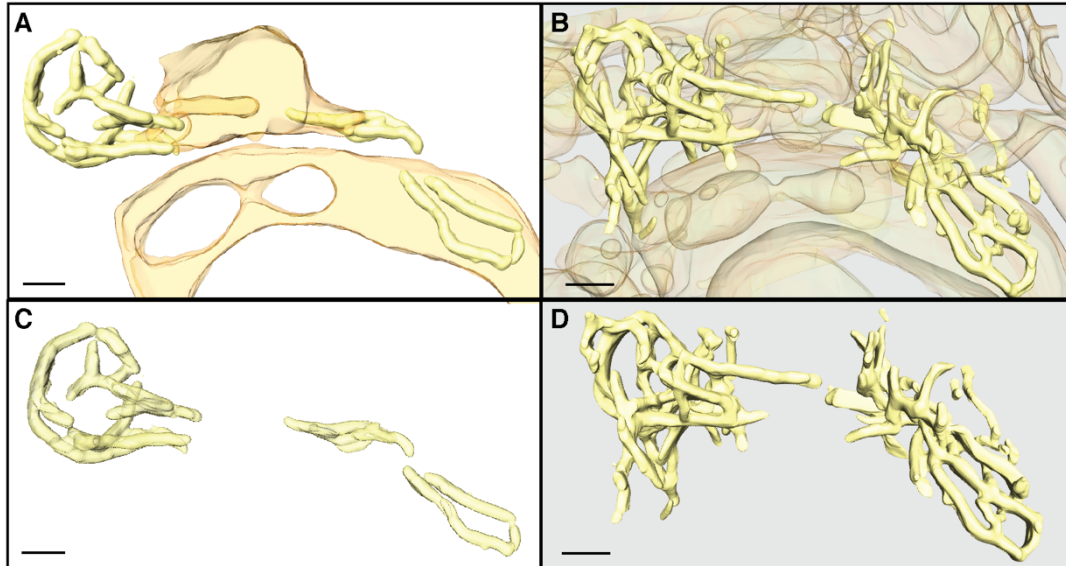


Fig. S6.

Comparison of machine-learning and manual segmentation of U2OS tomogram. (A) and (C) are isosurfaces generated from EMAN2 CNN segmentation where general ER structures are shown in (A) and only the narrow RE1 α subdomain tubes are shown in C. (B) and (D) are comparable views with smoothed isosurfaces generated manually using manual segmentation tools in Amira. A lot more structures are recognized by human eyes than are annotated by the neural network, especially at junctional regions. The manual segmentation in (B) and (D) therefore has higher degree of connectivity compared to (A) and (C). Scale bars = 100 nm.

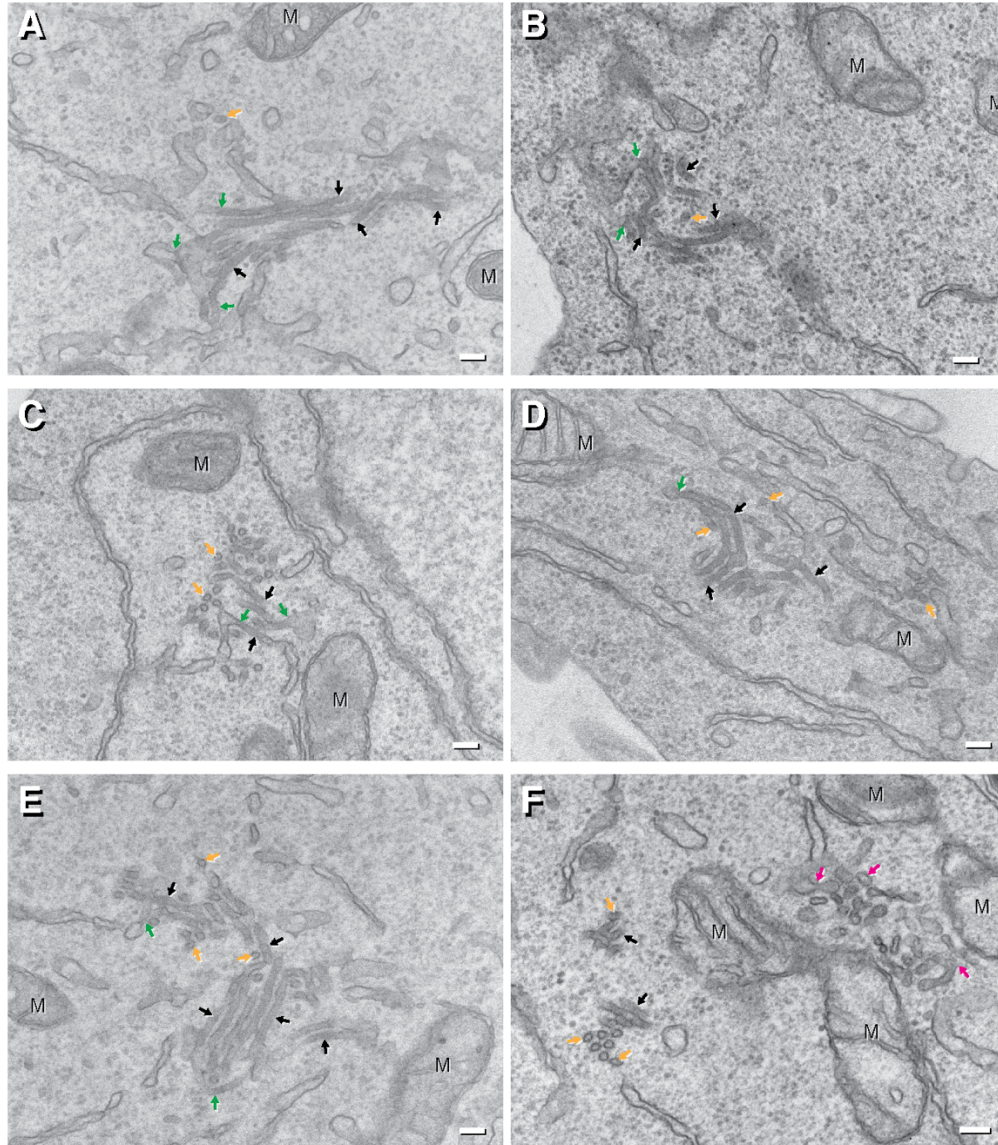


Fig. S7.

Rare instances of IRE1 α subdomain can be observed in stressed cells expressing inducible IRE1 α -GFP by conventional EM. (A-F) Micrographs of thin sections of Epon-embedded cells. Thin membrane structures with diameters of 30 ± 3 nm (\pm SD, n=89 measurements) can be observed as rectangular longitudinal (black arrows) and circular end-on cross-sections (orange arrows). These narrow membranes are connected to larger ER structures (diameters of 53 ± 20 nm; \pm SD, n=90 measurements) at junctions indicated by green arrows. Intriguingly, the lumens of these structures appear darker than surrounding ER lumen, indicative of higher protein density. Scale bar = 100 nm. M = mitochondria. These extremely narrow membrane tubes are morphologically distinct from ER exit sites (magenta arrows in F), which are finger-like protrusions with diameters of 35 ± 7 nm (n=20 measurements) consistent with ER-derived vesicles.

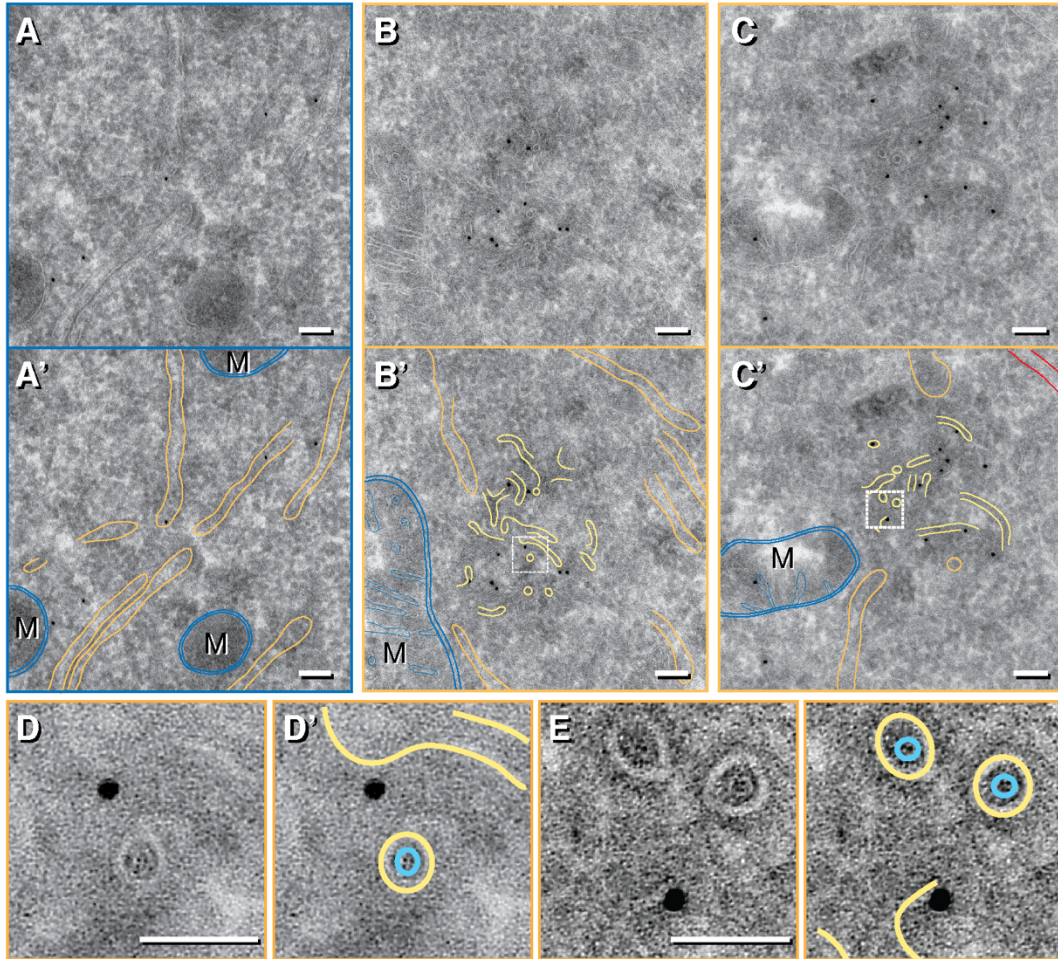


Fig. S8.

Additional example of visualization of IRE1 α subdomain by immunogold EM. (A, A') Micrograph of cell expressing IRE1 α -GFP epitope but not stressed, showing disperse and sparse immunogold particles labeling general ER tubules/sheets segmented in orange. M = mitochondria are segmented in blue. Scale bars = 100 nm. (B, B', C, C') Micrograph of immunogold-labeled stressed cells expressing IRE1 α -GFP epitope. Large clusters of gold particles localize to regions with narrow membrane structures (segmented in yellow). These narrow tubes have an averaged diameter of 26 ± 2 nm (error: standard deviation; n = 108 measurements) compared to surrounding ER structures segmented in orange with an averaged diameter of 51 ± 18 nm (error: standard deviation; n = 133 measurements). M = mitochondria are segmented in blue. Plasma membranes seen in C are segmented in red. Scale bars = 100 nm. Regions within white squares in B' and C' are enlarged in D and E, respectively. End-on cross sections of thin IRE1 α subdomain tubes appear as two roughly concentric rings, consistent with helical protein density within the lumen (cyan density). Scale bar = 50 nm.

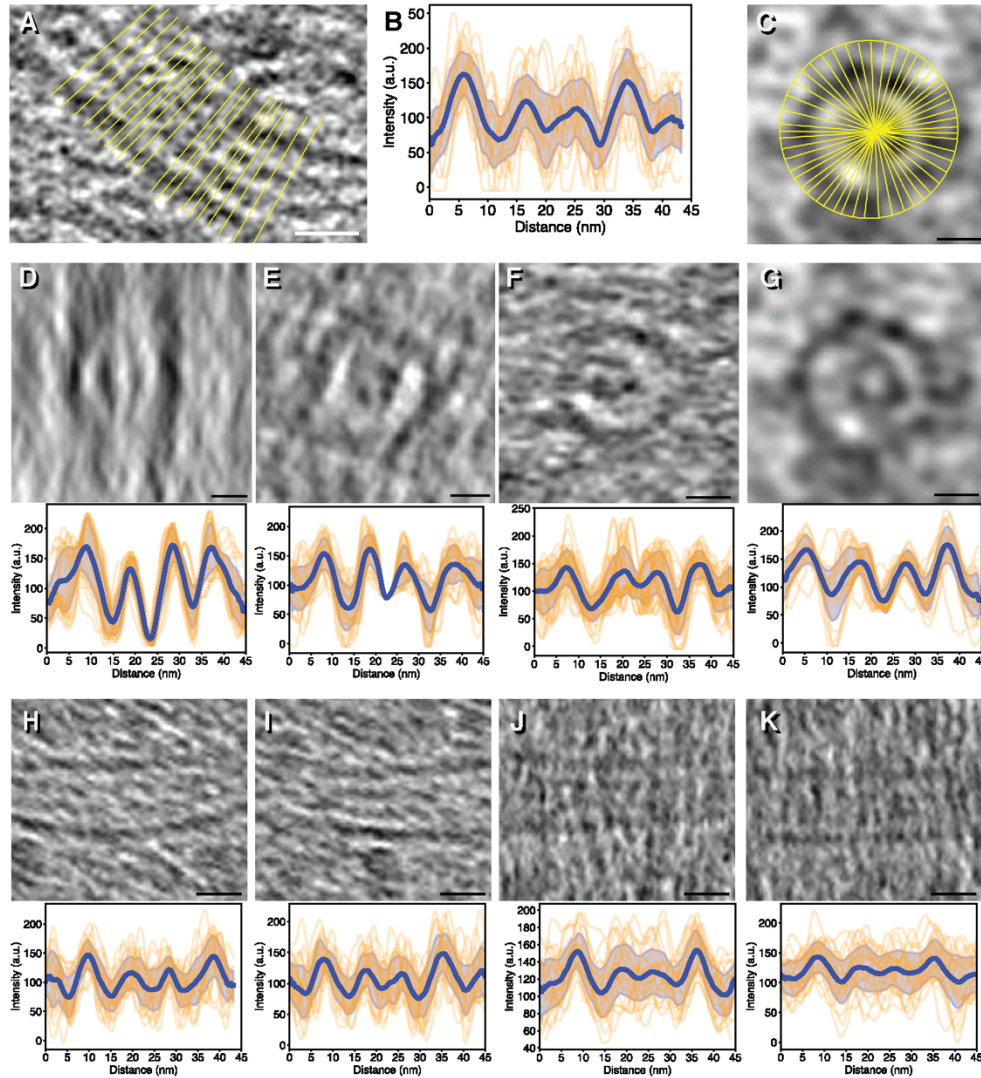


Fig. S9.

IRE1 α subdomain tubes in MEFs cells contain luminal protein density. (A) Example of how line profiles were drawn for IRE1 α subdomain longitudinal cross sections and resulting averaged line plot (B) showing four distinct peaks. (C) Example of how line profiles were drawn for IRE1 α subdomain end-on cross section depicted in Fig. 3B. (D-K) IRE1 α subdomain cross sections and corresponding resulting averaged line plots used to generate plot of averaged profiles and measure diameters shown in Fig. 3C. Blue lines with shaded error of the mean are the averaged trace for individual line plots aligned and averaged shown in orange. Scale bars = 20 nm.

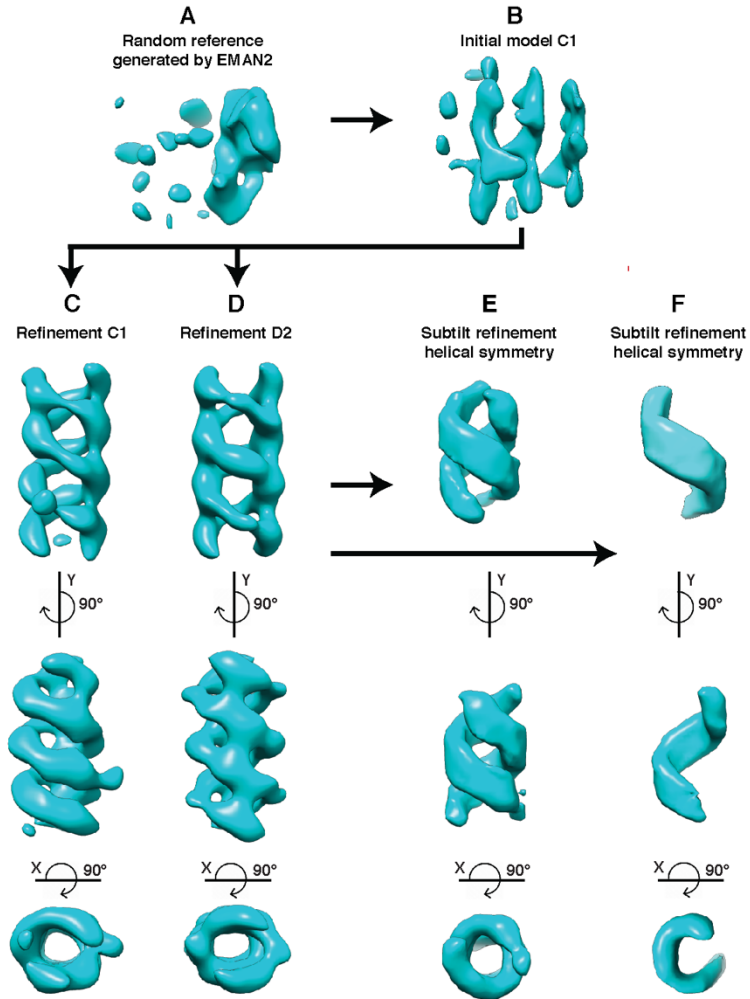


Fig. S10.

Subtomogram average workflow. (A) EMAN2 generated random reference. (B) Initial C1 model. (C) Refinement of the initial model in C1. (D) Refinement of the initial model in D2. This D2 average was used as a reference for all the following subtilt refinements, (E) helical symmetry (F) helical symmetry focused on one strand of the double-helical filament.

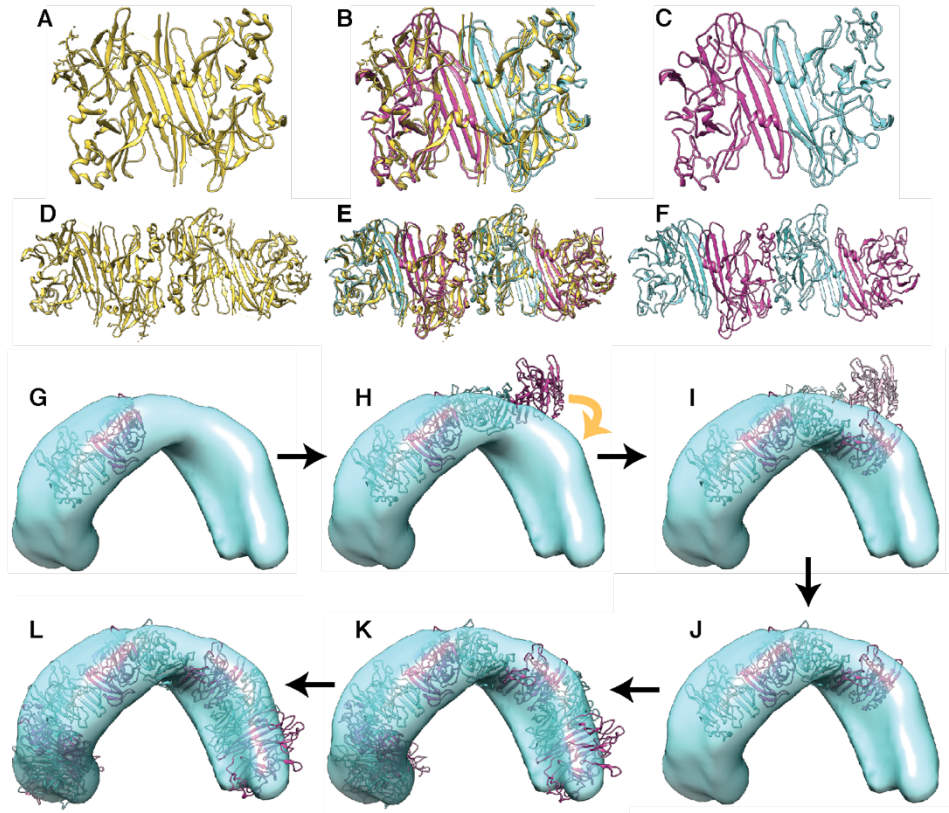


Fig. S11.

Generation of a modeled human active IRE1 α -LD oligomer. (A-F) comparison of the *S. cerevisiae* IRE1 luminal crystal structure (PDB:2BE1) used as a template for threading the human IRE1 α -LD sequence. (A) 2BE1 dimer. (B) 2BE1 superimposed with the threaded model of human IRE1 α -LD dimer shown in (C). (D-F) tetramers corresponding to (A-C). The modeled active human IRE1 α -LDs dimer (G) and tetramer (H) fitted into the map of one strand of the double helical filament. 97.7% of 10458 atoms fit inside the map in (G). Keeping the first dimer stationary, the dimer:dimer interface (IF2) was modified by changing the interface angle as indicated by arrow in (H) so that the second dimer also fit inside the map, resulting in a new tetramer shown in (I-J). The tetramer was then duplicated and propagated using the “Match” function in Chimera to generate a helix comprised of 9 monomers shown in (K), which completes one turn. (L) The helix is fitted as a rigid body to the map using the “Fit in map” function in Chimera, resulting in 84% of 47061 atoms fitting inside the volume.

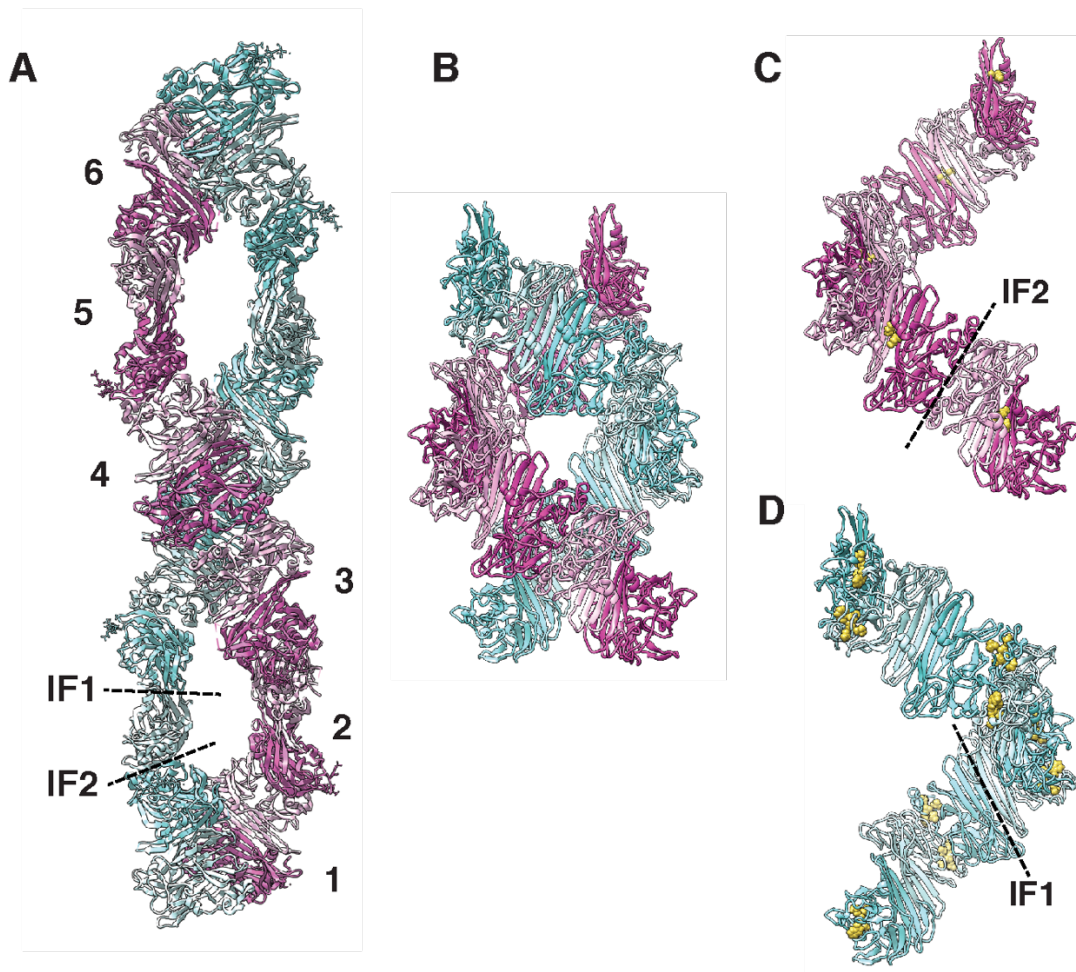


Fig. S12.

Comparison of *S. cerevisiae* IRE1-cLD 2BE1 and modeled active human IRE1 α -cLD oligomers. (A) Double helical oligomer found in the crystal structure of the *S. cerevisiae* IRE1-cLD with 12 dimers per double-helical turn and the putative unfolded protein binding groove facing outward. Numbers indicate individual dimers running along one helical filament. The dimer interface (IF1) and dimer:dimer interface (IF2) are shown as dashed lines. (B) The human IRE1 α -cLD double helix modelled and fitted to the sub-tomogram averaging map, showing 18 monomers per turn with the putative binding groove also facing outward. Individual strands of the human IRE1 α -LD double helix showing the IF1 residue K121 as yellow spheres in (C) and the IF2 residues WLLI (a.a. 359-362) as yellow spheres in (D). The human IRE1 α -cLD IF2 and IF1 are shown as dashed lines in (C) and (D), respectively. Mutation of both IF1 (19) and IF2 (14) residues were shown previously to abolish IRE1 α clustering and RNase activity.

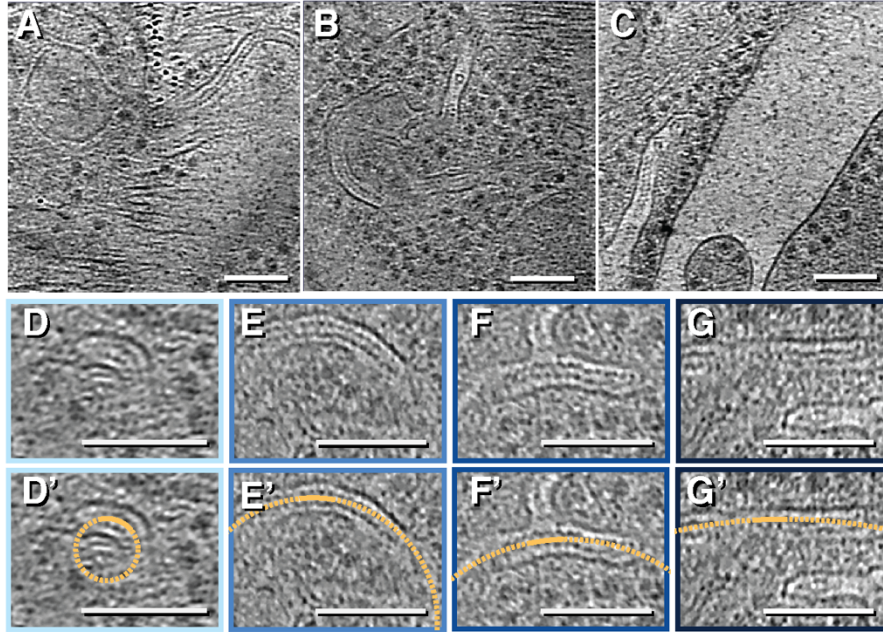


Fig. S13.

Example range of curvatures observed for IRE1 α subdomains. (A-C) Example regions from U2OS- IRE1 α -mNG cells showing IRE1 α subdomain tubes with varying degrees of curvature. Cropped regions exhibiting radii of curvature (ROC) ranging from 25-75 nm (D), 75-125 nm (E), 125-175 nm (F), and >175 nm (G) quantified and plotted in Fig. 4D. The outline color matches the bars in Fig. 4D, organized as increasing darkness corresponding to increasing ROC. A sample local curvature fit circle (dash orange circle) with ROC of 25 nm (D'), 100 nm (E'), 150 nm (F') and 400 nm (G') are shown for representative 25nm segments (solid orange arcs) within the view shown. All scale bars = 100 nm.

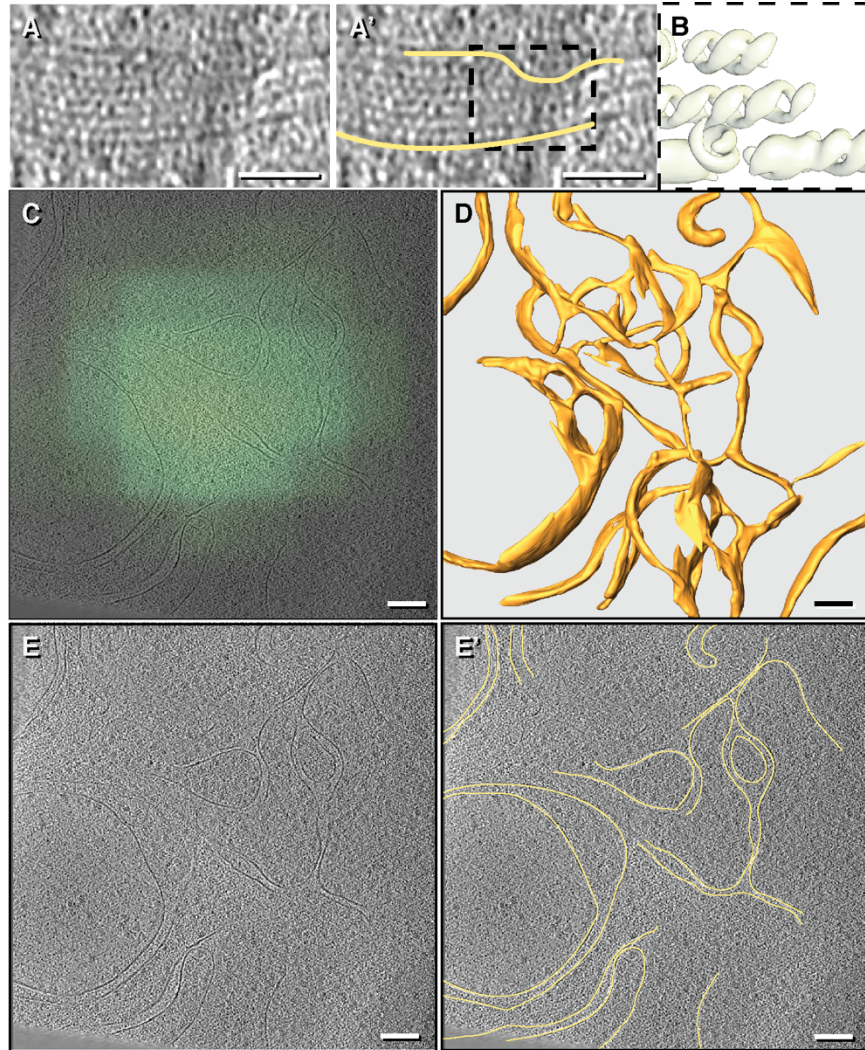


Fig. S14.

Anomaly in IRE1 α subdomains structures. (A, A') An example of an IRE1 α subdomain tube containing multiple juxtaped IRE α -LD filaments not separated by membrane (yellow). Scale bar = 20 nm (B) An isosurface of the averaged density mapped back into this region. (C) Overlay of cryo-light microscopy image and a representative slice of the reconstructed tomogram showing colocalization of IRE1 α -mNG foci to cell sub-regions with complex membrane topology and irregular inter-membrane diameters. Scale bar = 100 nm. (D) Segmentation of this putative precursor of IRE1 α subdomains with regular tube diameter, showing thin tubes connected by 3-ways junctions and enrichment of ER-fenestrations. (E, E') An example z slice of the membrane structures observed. Scale bars = 100 nm.

References and Notes

1. A. Helenius, T. Marquardt, I. Braakman, The endoplasmic reticulum as a protein-folding compartment. *Trends Cell Biol.* **2**, 227–231 (1992). [doi:10.1016/0962-8924\(92\)90309-B](https://doi.org/10.1016/0962-8924(92)90309-B) [Medline](#)
2. G. E. Karagöz, D. Acosta-Alvear, P. Walter, The unfolded protein response: Detecting and responding to fluctuations in the protein-folding capacity of the endoplasmic reticulum. *Cold Spring Harb. Perspect. Biol.* **11**, a033886 (2019). [doi:10.1101/cshperspect.a033886](https://doi.org/10.1101/cshperspect.a033886) [Medline](#)
3. K. Mori, W. Ma, M. J. Gething, J. Sambrook, A transmembrane protein with a cdc2+/CDC28-related kinase activity is required for signaling from the ER to the nucleus. *Cell* **74**, 743–756 (1993). [doi:10.1016/0092-8674\(93\)90521-Q](https://doi.org/10.1016/0092-8674(93)90521-Q) [Medline](#)
4. J. S. Cox, C. E. Shamu, P. Walter, Transcriptional induction of genes encoding endoplasmic reticulum resident proteins requires a transmembrane protein kinase. *Cell* **73**, 1197–1206 (1993). [doi:10.1016/0092-8674\(93\)90648-A](https://doi.org/10.1016/0092-8674(93)90648-A) [Medline](#)
5. I. Tabas, D. Ron, Integrating the mechanisms of apoptosis induced by endoplasmic reticulum stress. *Nat. Cell Biol.* **13**, 184–190 (2011). [doi:10.1038/ncb0311-184](https://doi.org/10.1038/ncb0311-184) [Medline](#)
6. J. H. Lin, H. Li, D. Yasumura, H. R. Cohen, C. Zhang, B. Panning, K. M. Shokat, M. M. Lavail, P. Walter, IRE1 signaling affects cell fate during the unfolded protein response. *Science* **318**, 944–949 (2007). [doi:10.1126/science.1146361](https://doi.org/10.1126/science.1146361) [Medline](#)
7. M. Lu, D. A. Lawrence, S. Marsters, D. Acosta-Alvear, P. Kimmig, A. S. Mendez, A. W. Paton, J. C. Paton, P. Walter, A. Ashkenazi, Opposing unfolded-protein-response signals converge on death receptor 5 to control apoptosis. *Science* **345**, 98–101 (2014). [doi:10.1126/science.1254312](https://doi.org/10.1126/science.1254312) [Medline](#)
8. T.-K. Chang, D. A. Lawrence, M. Lu, J. Tan, J. M. Harnoss, S. A. Marsters, P. Liu, W. Sandoval, S. E. Martin, A. Ashkenazi, Coordination between two branches of the unfolded protein response determines apoptotic cell fate. *Mol. Cell* **71**, 629–636.e5 (2018). [doi:10.1016/j.molcel.2018.06.038](https://doi.org/10.1016/j.molcel.2018.06.038) [Medline](#)
9. C. Hetz, K. Zhang, R. J. Kaufman, Mechanisms, regulation and functions of the unfolded protein response. *Nat. Rev. Mol. Cell Biol.* **21**, 421–438 (2020). [doi:10.1038/s41580-020-0250-z](https://doi.org/10.1038/s41580-020-0250-z) [Medline](#)
10. X. Z. Wang, H. P. Harding, Y. Zhang, E. M. Jolicoeur, M. Kuroda, D. Ron, Cloning of mammalian Ire1 reveals diversity in the ER stress responses. *EMBO J.* **17**, 5708–5717 (1998). [doi:10.1093/emboj/17.19.5708](https://doi.org/10.1093/emboj/17.19.5708) [Medline](#)
11. C. Sidrauski, P. Walter, The transmembrane kinase Ire1p is a site-specific endonuclease that initiates mRNA splicing in the unfolded protein response. *Cell* **90**, 1031–1039 (1997). [doi:10.1016/S0092-8674\(00\)80369-4](https://doi.org/10.1016/S0092-8674(00)80369-4) [Medline](#)
12. A. Bertolotti, Y. Zhang, L. M. Hendershot, H. P. Harding, D. Ron, Dynamic interaction of BiP and ER stress transducers in the unfolded-protein response. *Nat. Cell Biol.* **2**, 326–332 (2000). [doi:10.1038/35014014](https://doi.org/10.1038/35014014) [Medline](#)

13. B. M. Gardner, P. Walter, Unfolded proteins are Ire1-activating ligands that directly induce the unfolded protein response. *Science* **333**, 1891–1894 (2011). [doi:10.1126/science.1209126](https://doi.org/10.1126/science.1209126) [Medline](#)
14. G. E. Karagöz, D. Acosta-Alvear, H. T. Nguyen, C. P. Lee, F. Chu, P. Walter, An unfolded protein-induced conformational switch activates mammalian IRE1. *eLife* **6**, e30700 (2017). [doi:10.7554/eLife.30700](https://doi.org/10.7554/eLife.30700) [Medline](#)
15. M. M. U. Ali, T. Bagratuni, E. L. Davenport, P. R. Nowak, M. C. Silva-Santisteban, A. Hardcastle, C. McAndrews, M. G. Rowlands, G. J. Morgan, W. Aherne, I. Collins, F. E. Davies, L. H. Pearl, Structure of the Ire1 autophosphorylation complex and implications for the unfolded protein response. *EMBO J.* **30**, 894–905 (2011). [doi:10.1038/emboj.2011.18](https://doi.org/10.1038/emboj.2011.18) [Medline](#)
16. M. Calfon, H. Zeng, F. Urano, J. H. Till, S. R. Hubbard, H. P. Harding, S. G. Clark, D. Ron, IRE1 couples endoplasmic reticulum load to secretory capacity by processing the XBP-1 mRNA. *Nature* **415**, 92–96 (2002). [doi:10.1038/415092a](https://doi.org/10.1038/415092a) [Medline](#)
17. J. Hollien, J. S. Weissman, Decay of endoplasmic reticulum-localized mRNAs during the unfolded protein response. *Science* **313**, 104–107 (2006). [doi:10.1126/science.1129631](https://doi.org/10.1126/science.1129631) [Medline](#)
18. T. Aragón, E. van Anken, D. Pincus, I. M. Serafimova, A. V. Korennykh, C. A. Rubio, P. Walter, Messenger RNA targeting to endoplasmic reticulum stress signalling sites. *Nature* **457**, 736–740 (2009). [doi:10.1038/nature07641](https://doi.org/10.1038/nature07641) [Medline](#)
19. H. Li, A. V. Korennykh, S. L. Behrman, P. Walter, Mammalian endoplasmic reticulum stress sensor IRE1 signals by dynamic clustering. *Proc. Natl. Acad. Sci. U.S.A.* **107**, 16113–16118 (2010). [doi:10.1073/pnas.1010580107](https://doi.org/10.1073/pnas.1010580107) [Medline](#)
20. J. J. Credle, J. S. Finer-Moore, F. R. Papa, R. M. Stroud, P. Walter, On the mechanism of sensing unfolded protein in the endoplasmic reticulum. *Proc. Natl. Acad. Sci. U.S.A.* **102**, 18773–18784 (2005). [doi:10.1073/pnas.0509487102](https://doi.org/10.1073/pnas.0509487102) [Medline](#)
21. J. Zhou, C. Y. Liu, S. H. Back, R. L. Clark, D. Peisach, Z. Xu, R. J. Kaufman, The crystal structure of human IRE1 luminal domain reveals a conserved dimerization interface required for activation of the unfolded protein response. *Proc. Natl. Acad. Sci. U.S.A.* **103**, 14343–14348 (2006). [doi:10.1073/pnas.0606480103](https://doi.org/10.1073/pnas.0606480103) [Medline](#)
22. A. V. Korennykh, P. F. Egea, A. A. Korostelev, J. Finer-Moore, C. Zhang, K. M. Shokat, R. M. Stroud, P. Walter, The unfolded protein response signals through high-order assembly of Ire1. *Nature* **457**, 687–693 (2009). [doi:10.1038/nature07661](https://doi.org/10.1038/nature07661) [Medline](#)
23. D. Ricci, I. Marrocco, D. Blumenthal, M. Dibos, D. Eletto, J. Vargas, S. Boyle, Y. Iwamoto, S. Chomistek, J. C. Paton, A. W. Paton, Y. Argon, Clustering of IRE1 α depends on sensing ER stress but not on its RNase activity. *FASEB J.* **33**, 9811–9827 (2019). [doi:10.1096/fj.201801240RR](https://doi.org/10.1096/fj.201801240RR) [Medline](#)
24. V. Belyy, N.-H. Tran, P. Walter, Quantitative microscopy reveals dynamics and fate of clustered IRE1 α . *Proc. Natl. Acad. Sci. U.S.A.* **117**, 1533–1542 (2020). [doi:10.1073/pnas.1915311117](https://doi.org/10.1073/pnas.1915311117) [Medline](#)
25. W. F. Tivol, A. Briegel, G. J. Jensen, An improved cryogen for plunge freezing. *Microsc.*

- Microanal.* **14**, 375–379 (2008). [doi:10.1017/S1431927608080781](https://doi.org/10.1017/S1431927608080781) [Medline](#)
26. A. Briegel, S. Chen, A. J. Koster, J. M. Plitzko, C. L. Schwartz, G. J. Jensen, Correlated light and electron cryo-microscopy. *Methods Enzymol.* **481**, 317–341 (2010). [doi:10.1016/S0076-6879\(10\)81013-4](https://doi.org/10.1016/S0076-6879(10)81013-4) [Medline](#)
27. S. D. Carter, S. K. Mageswaran, Z. J. Farino, J. I. Mamede, C. M. Oikonomou, T. J. Hope, Z. Freyberg, G. J. Jensen, Distinguishing signal from autofluorescence in cryogenic correlated light and electron microscopy of mammalian cells. *J. Struct. Biol.* **201**, 15–25 (2018). [doi:10.1016/j.jsb.2017.10.009](https://doi.org/10.1016/j.jsb.2017.10.009) [Medline](#)
28. J. Yang, Y. Zhang, I-TASSER server: New development for protein structure and function predictions. *Nucleic Acids Res.* **43**, W174–W181 (2015). [doi:10.1093/nar/gkv342](https://doi.org/10.1093/nar/gkv342) [Medline](#)
29. N. Borgese, M. Francolini, E. Snapp, Endoplasmic reticulum architecture: Structures in flux. *Curr. Opin. Cell Biol.* **18**, 358–364 (2006). [doi:10.1016/j.ceb.2006.06.008](https://doi.org/10.1016/j.ceb.2006.06.008) [Medline](#)
30. J. Nixon-Abell, C. J. Obara, A. V. Weigel, D. Li, W. R. Legant, C. S. Xu, H. A. Pasolli, K. Harvey, H. F. Hess, E. Betzig, C. Blackstone, J. Lippincott-Schwartz, Increased spatiotemporal resolution reveals highly dynamic dense tubular matrices in the peripheral ER. *Science* **354**, eaaf3928 (2016). [doi:10.1126/science.aaf3928](https://doi.org/10.1126/science.aaf3928) [Medline](#)
31. M. J. Phillips, G. K. Voeltz, Structure and function of ER membrane contact sites with other organelles. *Nat. Rev. Mol. Cell Biol.* **17**, 69–82 (2016). [doi:10.1038/nrm.2015.8](https://doi.org/10.1038/nrm.2015.8) [Medline](#)
32. S. Schuck, W. A. Prinz, K. S. Thorn, C. Voss, P. Walter, Membrane expansion alleviates endoplasmic reticulum stress independently of the unfolded protein response. *J. Cell Biol.* **187**, 525–536 (2009). [doi:10.1083/jcb.200907074](https://doi.org/10.1083/jcb.200907074) [Medline](#)
33. S. Asano, B. D. Engel, W. Baumeister, In situ cryo-electron tomography: A post-reductionist approach to structural biology. *J. Mol. Biol.* **428**, 332–343 (2016). [doi:10.1016/j.jmb.2015.09.030](https://doi.org/10.1016/j.jmb.2015.09.030) [Medline](#)
34. T. Cui-Wang, C. Hanus, T. Cui, T. Helton, J. Bourne, D. Watson, K. M. Harris, M. D. Ehlers, Local zones of endoplasmic reticulum complexity confine cargo in neuronal dendrites. *Cell* **148**, 309–321 (2012). [doi:10.1016/j.cell.2011.11.056](https://doi.org/10.1016/j.cell.2011.11.056) [Medline](#)
35. M. Sanches, N. M. Duffy, M. Talukdar, N. Thevakumaran, D. Chiovitti, M. D. Canny, K. Lee, I. Kurinov, D. Uehling, R. Al-awar, G. Poda, M. Prakesch, B. Wilson, V. Tam, C. Schweitzer, A. Toro, J. L. Lucas, D. Vuga, L. Lehmann, D. Durocher, Q. Zeng, J. B. Patterson, F. Sicheri, Structure and mechanism of action of the hydroxy-aryl-aldehyde class of IRE1 endoribonuclease inhibitors. *Nat. Commun.* **5**, 4202 (2014). [doi:10.1038/ncomms5202](https://doi.org/10.1038/ncomms5202) [Medline](#)
36. M. Puhka, M. Joensuu, H. Vihinen, I. Belevich, E. Jokitalo, Progressive sheet-to-tubule transformation is a general mechanism for endoplasmic reticulum partitioning in dividing mammalian cells. *MBoC* **23**, 2424–2432 (2012). [doi:10.1091/mbc.e10-12-0950](https://doi.org/10.1091/mbc.e10-12-0950) [Medline](#)
37. T. Shemesh, R. W. Klemm, F. B. Romano, S. Wang, J. Vaughan, X. Zhuang, H. Tukachinsky, M. M. Kozlov, T. A. Rapoport, A model for the generation and interconversion of ER morphologies. *Proc. Natl. Acad. Sci. U.S.A.* **111**, E5243–E5251 (2014). [doi:10.1073/pnas.1419997111](https://doi.org/10.1073/pnas.1419997111) [Medline](#)

38. N.-H. Tran, S. Carter, A. De Mazière, A. Ashkenazi, J. Klumperman, P. Walter, G. Jensen, Analysis code and quantification for publication “The stress-sensing domain of activated IRE1 α forms helical filaments in narrow ER membrane tubes.” Zenodo (2021); <http://doi.org/10.5281/zenodo.5030935>
39. S. Q. Zheng, B. Keszthelyi, E. Branlund, J. M. Lyle, M. B. Braunfeld, J. W. Sedat, D. A. Agard, UCSF tomography: An integrated software suite for real-time electron microscopic tomographic data collection, alignment, and reconstruction. *J. Struct. Biol.* **157**, 138–147 (2007). [doi:10.1016/j.jsb.2006.06.005](https://doi.org/10.1016/j.jsb.2006.06.005) [Medline](#)
40. D. N. Mastronarde, Automated electron microscope tomography using robust prediction of specimen movements. *J. Struct. Biol.* **152**, 36–51 (2005). [doi:10.1016/j.jsb.2005.07.007](https://doi.org/10.1016/j.jsb.2005.07.007) [Medline](#)
41. J. R. Kremer, D. N. Mastronarde, J. R. McIntosh, Computer visualization of three-dimensional image data using IMOD. *J. Struct. Biol.* **116**, 71–76 (1996). [doi:10.1006/jsbi.1996.0013](https://doi.org/10.1006/jsbi.1996.0013) [Medline](#)
42. J. I. Agulleiro, J. J. Fernandez, Fast tomographic reconstruction on multicore computers. *Bioinformatics* **27**, 582–583 (2011). [doi:10.1093/bioinformatics/btq692](https://doi.org/10.1093/bioinformatics/btq692) [Medline](#)
43. M. Chen, W. Dai, S. Y. Sun, D. Jonasch, C. Y. He, M. F. Schmid, W. Chiu, S. J. Ludtke, Convolutional neural networks for automated annotation of cellular cryo-electron tomograms. *Nat. Methods* **14**, 983–985 (2017). [doi:10.1038/nmeth.4405](https://doi.org/10.1038/nmeth.4405) [Medline](#)
44. J. W. Slot, H. J. Geuze, Cryosectioning and immunolabeling. *Nat. Protoc.* **2**, 2480–2491 (2007). [doi:10.1038/nprot.2007.365](https://doi.org/10.1038/nprot.2007.365) [Medline](#)
45. S. J. Scales, N. Gupta, A. M. De Mazière, G. Posthuma, C. P. Chiu, A. A. Pierce, K. Hötzel, J. Tao, O. Foreman, G. Koukos, F. Oltrabella, J. Klumperman, W. Lin, A. S. Peterson, Apolipoprotein L1-specific antibodies detect endogenous APOL1 inside the endoplasmic reticulum and on the plasma membrane of podocytes. *J. Am. Soc. Nephrol.* **31**, 2044–2064 (2020). [doi:10.1681/ASN.2019080829](https://doi.org/10.1681/ASN.2019080829) [Medline](#)
46. M. Chen, J. M. Bell, X. Shi, S. Y. Sun, Z. Wang, S. J. Ludtke, A complete data processing workflow for cryo-ET and subtomogram averaging. *Nat. Methods* **16**, 1161–1168 (2019). [doi:10.1038/s41592-019-0591-8](https://doi.org/10.1038/s41592-019-0591-8) [Medline](#)
47. A. Waterhouse, M. Bertoni, S. Bienert, G. Studer, G. Tauriello, R. Gumienny, F. T. Heer, T. A. P. de Beer, C. Rempfer, L. Bordoli, R. Lepore, T. Schwede, SWISS-MODEL: Homology modelling of protein structures and complexes. *Nucleic Acids Res.* **46**, W296–W303 (2018). [doi:10.1093/nar/gky427](https://doi.org/10.1093/nar/gky427) [Medline](#)
48. E. F. Pettersen, T. D. Goddard, C. C. Huang, G. S. Couch, D. M. Greenblatt, E. C. Meng, T. E. Ferrin, UCSF Chimera—A visualization system for exploratory research and analysis. *J. Comput. Chem.* **25**, 1605–1612 (2004). [doi:10.1002/jcc.20084](https://doi.org/10.1002/jcc.20084) [Medline](#)
49. J. Schindelin, I. Arganda-Carreras, E. Frise, V. Kaynig, M. Longair, T. Pietzsch, S. Preibisch, C. Rueden, S. Saalfeld, B. Schmid, J.-Y. Tinevez, D. J. White, V. Hartenstein, K. Eliceiri, P. Tomancak, A. Cardona, Fiji: An open-source platform for biological-image analysis. *Nat. Methods* **9**, 676–682 (2012). [doi:10.1038/nmeth.2019](https://doi.org/10.1038/nmeth.2019) [Medline](#)
50. K. Mitra, I. Ubarretxena-Belandia, T. Taguchi, G. Warren, D. M. Engelman, Modulation of

the bilayer thickness of exocytic pathway membranes by membrane proteins rather than cholesterol. *Proc. Natl. Acad. Sci. U.S.A.* **101**, 4083–4088 (2004).

[doi:10.1073/pnas.0307332101](https://doi.org/10.1073/pnas.0307332101) [Medline](#)

51. H. Fischer, I. Polikarpov, A. F. Craievich, Average protein density is a molecular-weight-dependent function. *Protein Sci.* **13**, 2825–2828 (2004). [doi:10.1110/ps.04688204](https://doi.org/10.1110/ps.04688204)

[Medline](#)